JOURNAL OF GUIDANCE, CONTROL, AND DYNAMICS
Vol. 32, No. 2, March–April 2009

Circulating Eccentric Orbits Around Planetary Moons

Ryan P. Russell* and Adam T. Brinckerhoff†
Georgia Institute of Technology, Atlanta, Georgia 30332-0150

DOI: 10.2514/1.38593

Eccentric orbits in the third-body perturbed problem are evaluated in the context of planetary-moon missions. All possible motion in the doubly averaged problem is reviewed and concisely summarized via contour plots. Special attention is paid to the well-known class of orbits that cycle between low and high eccentricity while circulating in argument of periapse. Applying the doubly averaged assumptions, the maximum sustainable inclinations and eccentricities for long-term circulating ballistic orbits are found and discussed for the dimensioned systems at Ganymede, Europa, Titan, Enceladus, and several other planetary moons. The full-cycle periods of the circulations and librations are reduced to quadratures that are functions only of the two integrals of motion and the moon and orbiter mean motions. In the specific case of Ganymede, higher-fidelity models are considered to analyze the validity of the doubly averaged assumptions. Families of stable long-repeat-cycle periodic orbits are demonstrated in the unaveraged Hill-plus-nonspherical-potential model. Several point designs are considered in a full ephemeris model, and promising results include long-term ephemeris-stable orbits that enjoy maximum inclinations above 60 deg. These circulating "ball-of-yarn" orbits cycle between high and low eccentricities while distributing close approaches throughout the moon's surface.

Nomenclature

a, e, i, ω, Ω, υ	=	classical orbital elements: semimajor axis, eccentricity, inclination, argument of periapse, longitude of ascending node, and true anomaly
alt	=	altitude
a_s	=	moon semimajor axis
b_1, b_2	=	stability indices
C	=	Jacobi integral of motion
$C_{n,m}$, $S_{n,m}$	=	nth-degree and mth-order nonzonal gravity-field coefficients
C_1, C_2	=	integrals of motion in the doubly averaged system
J_n	=	nth-degree zonal gravity-field coefficient
N_s	=	moon mean motion
n	=	spacecraft mean motion
R	=	moon radius
r	=	radius magnitude of the spacecraft position
r_p	=	spacecraft periapse
T	=	spacecraft period
T_c	=	full contour cycle period
T_s	=	moon period
t	=	time
U	=	nonspherical gravity potential
x, y, z, u, v, w	=	rotating body-fixed state components
Γ	=	potential function
ε	=	small number
μ_p	=	planet gravitational parameter
μ_s	=	moon gravitational parameter

Presented as Paper AAS 08-181 at the AAS/AIAA Space Flight Mechanics Meeting, Galveston, TX, January 2008; received 16 May 2008; revision received 14 October 2008; accepted for publication 14 October 2008.

*Assistant Professor, Guggenheim School of Aerospace Engineering, 270 Ferst Drive; ryan.russell@gatech.edu. Member AIAA.

†Graduate Student, Guggenheim School of Aerospace Engineering; adam.brinckerhoff@gmail.com; Student Member AIAA.

I. Introduction

THE topic of science-orbit design around planetary moons is broad and has been the subject of many studies in recent years. To ensure global coverage, adequate surface mapping, and tidal bulge detection, science orbits are generally required to have high inclination, low altitude, and low eccentricity. Unfortunately, it is well known that most orbits about planetary satellites with these properties will eventually impact the satellite's surface due to dynamic instability from the third-body perturbation. Although low-altitude near-polar orbits are unstable and expensive to achieve in many cases, eccentric high-altitude orbits have received much less attention in terms of mission-design applications. One recent application involves constellation design at the Earth's moon [1], noting that the averaged third-body dynamics predict the existence of medium-inclination, stable, eccentric frozen orbits. A second class of orbits predicted by the averaged third-body dynamics [2], and further demonstrated as periodic orbits in the unaveraged third-body problem [3,4], is the circulating and librating class that indefinitely cycle between various degrees of high and low eccentricities. Although these orbits have been observed and documented in the normalized Hill's problem and a few dimensioned cases, including the Europa–Jupiter system, their general mission-design application has yet to be fully explored. In this study we review all types of motion predicted in the doubly averaged third-body problem, with particular emphasis on eccentric orbits, regions of validity for doubly averaged motion, and implications of the different time and distance scales associated with planetary moons of interest. In particular, we choose Ganymede as a promising application for these circulating eccentric orbits, and several examples are demonstrated. The doubly averaged assumptions are verified with the identification of periodic orbits in the unaveraged model [4], and the preliminary robustness of the orbit designs to realistic force perturbations is verified with ephemeris propagations.

Although low-altitude near-circular orbits are quite sensitive to nonspherical gravity effects, the inclusion of higher-order terms is found to be a second-order effect for high-altitude eccentric orbits. The largely analytical averaging techniques from [2] only include point-mass effects of the bodies and [5–7] consider a few dominant nonspherical terms, especially in the case of the circular orbits. Although the inclusion of the higher-order terms may prove to be difficult using averaging techniques, the periodic-orbit approach implemented in this study is amenable to including terms of arbitrary order, even in the case of a highly irregularly shaped body [4]. The rapid identification of the periodic orbits in a full gravity field is well

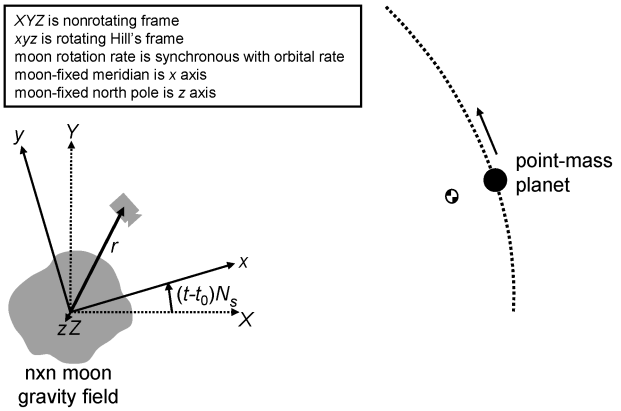

Fig. 1 Hill's model plus $n \times n$ potential model.

suited for future Monte Carlo analyses that will certainly be required to investigate gravity-field sensitivities.

II. Model Overview

The classic restricted three-body model assumes that the moon and planet are point masses and that they orbit their common center with a constant radius. Hill's model is the limiting case in which the moon to planet mass ratio approaches zero.[‡] This assumption results in a tidal force field that is symmetric about the plane passing through the moon center and perpendicular to the planet–moon line [2]. Hill's model becomes more valid as the mass ratio and spacecraft-to-moon distance decrease. By using Hill's model, the normalized equations of motion remain unchanged for all planetary-moon systems, and the dimensioned states for specific moon systems are found simply through the unnormalization process.

The dynamical model for the Hill problem superimposed by an $n \times n$ spherical harmonic moon gravity field is depicted in Fig. 1. Given the additional assumption that the rotation of the moon is synchronous with its orbital period, the moon-fixed reference frame is identical to the moon-centered rotating Hill's frame. Periodic orbits in this model represent dynamic equilibria in the unaveraged equations, and they are relied upon in this study to verify stability and motion predictions from the simplified doubly averaged system.

Table 1 gives the dimensioned parameters and associated normalized Hill's model units for a specific application at Ganymede. For cases including nonspherical Ganymede gravity terms, Appendix A includes a representative 4×4 Ganymede gravity field. The J_2 and C_{22} terms were estimated with reasonable confidence based on Galileo flyby data, and the remaining terms are simply representative of an expected field.

The equations of motion for the Hill's-plus-full-gravity model (see Fig. 1) are given in Eq. (1):

$$\ddot{x} = 2N_s v + \partial\Gamma/\partial x \qquad \ddot{y} = -2N_s u + \partial\Gamma/\partial y \qquad \ddot{z} = \partial\Gamma/\partial z \tag{1}$$

The potential function Γ is introduced in Eq. (2), in which U is the contribution due to the nonspherical moon, and it is expressed via the standard spherical harmonic expansion [8]. Typically, canonical units [length unit (LU) and time unit (TU)] are derived based on normalizing the moon mean motion and gravitational parameter N_s and μ_s, respectively, to unity. Figure 1 illustrates the geometry

$$\Gamma = \frac{1}{2}N_S^2(3x^2 - z^2) + \frac{\mu_s}{r} + U \qquad r = \sqrt{x^2 + y^2 + z^2} \tag{2}$$

The system is Hamiltonian and admits C, an integral of motion given in Eq. (3) that is analogous to the Jacobi constant:

$$C = 2\Gamma - (u^2 + v^2 + w^2) \tag{3}$$

[‡]Formally, the Hill approximation requires $(\mu_s/\mu_p)^{1/3} \ll 1$.

Table 1 Jupiter–Ganymede system parameters

Parameter	Value
Ganymede gravitational parameter	9886.99742842995 km^3/s^2
Jupiter gravitational parameter	1.26618626797685e8 km^3/s^2
Jupiter—Ganymede distance	1.0704e6 km
Ganymede mean radius	2631.2 km
Hill's normalized time unit (derived)	98,413.2095723724 s
Hill's normalized length unit (derived)	45,749.9268762215 km
System mean motion (derived)	1.016123754468760e-5 rad/s

In the case of a point-mass moon, a reduction of the system leads to the doubly averaged model in which the Hill's model potential is averaged twice: once over one spacecraft orbit and once over one moon orbit. The basic averaging assumption is that the spacecraft period is much smaller than the moon period. Typically, an order-of-magnitude difference in these periods justifies the use of the averaging approximation [7]. In the current study, we examine a range of system to spacecraft period ratios, evaluate the validity of the underlying averaging assumptions, and interpret the implications of this ratio to the broader context of mission design. When the equations of motion from Eq. (1) are formulated using the partial derivatives of the potential and Lagrange's planetary equations [2,7,9], the doubly averaged system leads to Eqs. (4–8):

$$\frac{da}{dt} = 0 \tag{4}$$

$$\frac{de}{dt} = \frac{15}{8}\frac{N_S^2}{n}e\sqrt{1-e^2}\sin^2 i \sin 2\omega \tag{5}$$

$$\frac{di}{dt} = -\frac{15}{16}\frac{N_S^2}{n}\frac{e^2}{\sqrt{1-e^2}}\sin 2i \sin 2\omega \tag{6}$$

$$\frac{d\omega}{dt} = \frac{3}{8}\frac{N_S^2}{n} \times \frac{1}{\sqrt{1-e^2}}[5\cos^2 i - 1 + 5\sin^2 i \cos 2\omega + e^2(1 - 5\cos 2\omega)] \tag{7}$$

$$\frac{d\Omega}{dt} = -\frac{3}{8}\frac{N_S^2}{n}\frac{\cos i}{\sqrt{1-e^2}}(2 + 3e^2 - 5e^2\cos 2\omega) \tag{8}$$

Selected ephemeris propagations are carried out to demonstrate the robustness of simplified-model solutions to perturbations associated with realistic force models. The ephemeris states of the planets, moons, and the sun are based on publicly available data from the Jet Propulsion Laboratory.[§] The body poles and prime meridians are based on the most recent data from the International Astronomical Union (IAU) working group on cartographic coordinates and rotational elements of the planets and satellites [10].

III. Doubly Averaged Third-Body System

The first-order dynamics of orbiters in the vicinity of point-mass planetary moons are captured nicely through averaging techniques that reduce the problem's dimension from six to three, enabling a

[§]Data available online at http://naif.jpl.nasa.gov/naif/spiceconcept.html, ftp://naif.jpl.nasa.gov/pub/naif/generic_kernels/spk/planets/a_old_versions/de414.bsp, ftp://naif.jpl.nasa.gov/pub/naif/generic_kernels/spk/satellites/jup230.bsp, and ftp://naif.jpl.nasa.gov/pub/naif/generic_kernels/pck/pck00008.tpc [retrieved 4 December 2008].

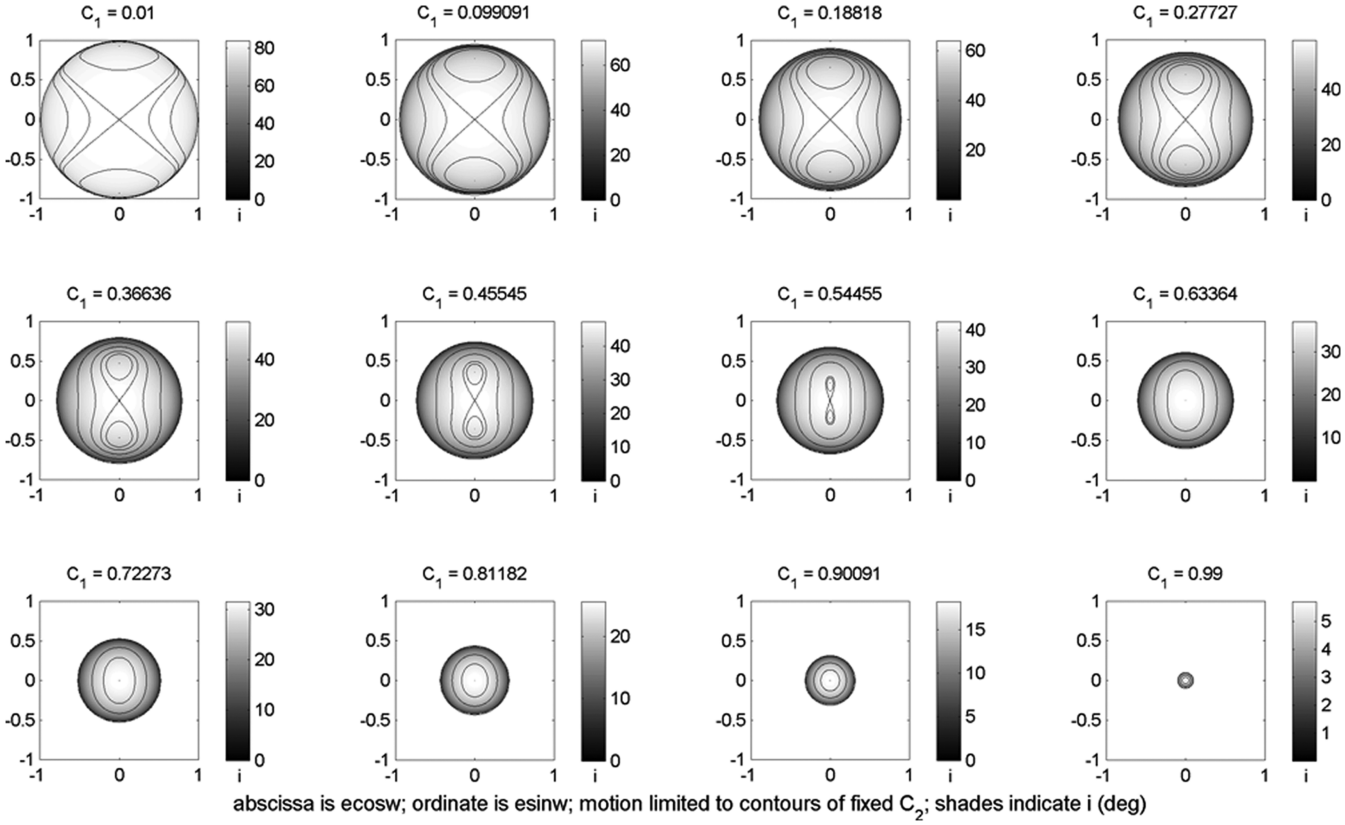

Fig. 2 Overview of possible orbital motion in the doubly averaged system.

thorough characterization of possible motion. For details on studies that rely on averaging, see [2,5,7,11–13], for example.

From Eqs. (4–8), note that semimajor axis is constant and the evolutions of eccentricity, inclination, and argument of periapse do not depend on longitude of the ascending node. Therefore, the basic characteristics of the orbit are practically reduced to the three variables e, i, and ω. Further, Broucke [2] shows that the reduced system includes two constant integrals of motion shown in Eqs. (9) and (10):

$$C_1 = (1 - e^2)\cos^2 i \tag{9}$$

$$C_2 = e^2(2/5 - \sin^2 i \sin^2 \omega) \tag{10}$$

Therefore, given an initial state for e, i, and ω, the system is reduced to 1 degree of freedom, as it is confined to remain on constant contours of C_1 and C_2. Figure 2 captures all types of motion allowed based on the feasible values of C_1 and C_2. The x axis on each of the plots is $e\cos\omega$ and the y axis is $e\sin\omega$. Therefore, the plot can be thought of in polar coordinates in which the eccentricity magnitude is the radius coordinate and the argument of periapse is the angle. Each subplot represents a constant value of C_1, as indicated in the subplot title. Note that C_1 can take on any value in the range from 0–1, and the C_2 range depends directly on C_1 (see [2] for details about the feasible regions of the C_1–C_2 plane). Contours of constant-C_2 values are illustrated on each subplot. The figure-eight-shaped contour in each plot reflects a C_2 of approximately zero ($\varepsilon > 0$), whereas the remaining contours are distributed among feasible values based on the given C_1.

If a spacecraft is initiated with a particular C_1 and C_2, then its motion is limited to the corresponding contour line, as long as no thrusting occurs. The rate at which the spacecraft moves around the contour line is influenced by a; however, the shape of the contour lines is independent of a. Inclination is indicated by different shades and is independent of the contour lines. Inverse of eccentricity, inclination finds its maximum at the center of each plot and its minimum (0 deg) along the outer circumference. Thus, as the system moves along the constant-C_2 lines, e, i, and ω change accordingly. Note that eccentricities ranging from 0–1 are feasible in the limit as C_1 approaches zero, whereas only $e = 0$ is valid in the limit as C_1 approaches one.

The motion illustrated in Fig. 2 is characterized by two basic features. When $C_1 > 3/5$, all contour lines circulate around the center of the plot; therefore, the argument of periapse circulates. The shape of the contours is circular toward the center and the boundary of each plot, whereas the interior regions find vertically elongated contours, indicating that the eccentricity will grow and shrink during each pass around the contour. Following a bifurcation at $C_1 = 3/5$, two islands emerge and move away from the center as C_1 decreases. Figure 3 shows this specific range of motion in a similar fashion to Fig. 2, with the addition of the normalized full-cycle contour period T_c, to be discussed later. Here, the motion is restricted to either librate around one of the islands or circulate around both islands. A frozen orbit exists at the center of each island that is stable because the neighboring orbits simply librate with near-constant eccentricity and argument of periapse. The two frozen orbits are represented on each plot by contours that appear as small dots above and below the origin, and the ovular contours around them represent possible librating orbits. For circulating orbits when $C_1 < 3/5$, note that the maximum inclination occurs when $e \sim 0$ and each cycle around the contour leads to maximum eccentricity at the top and bottom of each plot (corresponding to $\omega = \pm 90$ deg). For $e = 0$, the emergence of the islands (the bifurcation at $C_1 = 3/5$) corresponds to a stability boundary of $i \sim 39$ deg. Thus, all initially circular orbits with $i >$ 39 deg will repeatedly grow and shrink in e as the contours require either a librating or circulating cycle around one or both islands, respectively.

As an example, if a spacecraft starts with $(e_0, i_0, \omega_0) =$ $(0.001, 56.8\,\text{deg}, 0\,\text{deg})$, then $C_1 \sim 0.3$. Figure 4 shows that the resulting contour ♣ circulates around both islands, and e and i range from ~0 to ~0.7 and ~39 to ~56.8 deg, respectively. This type of

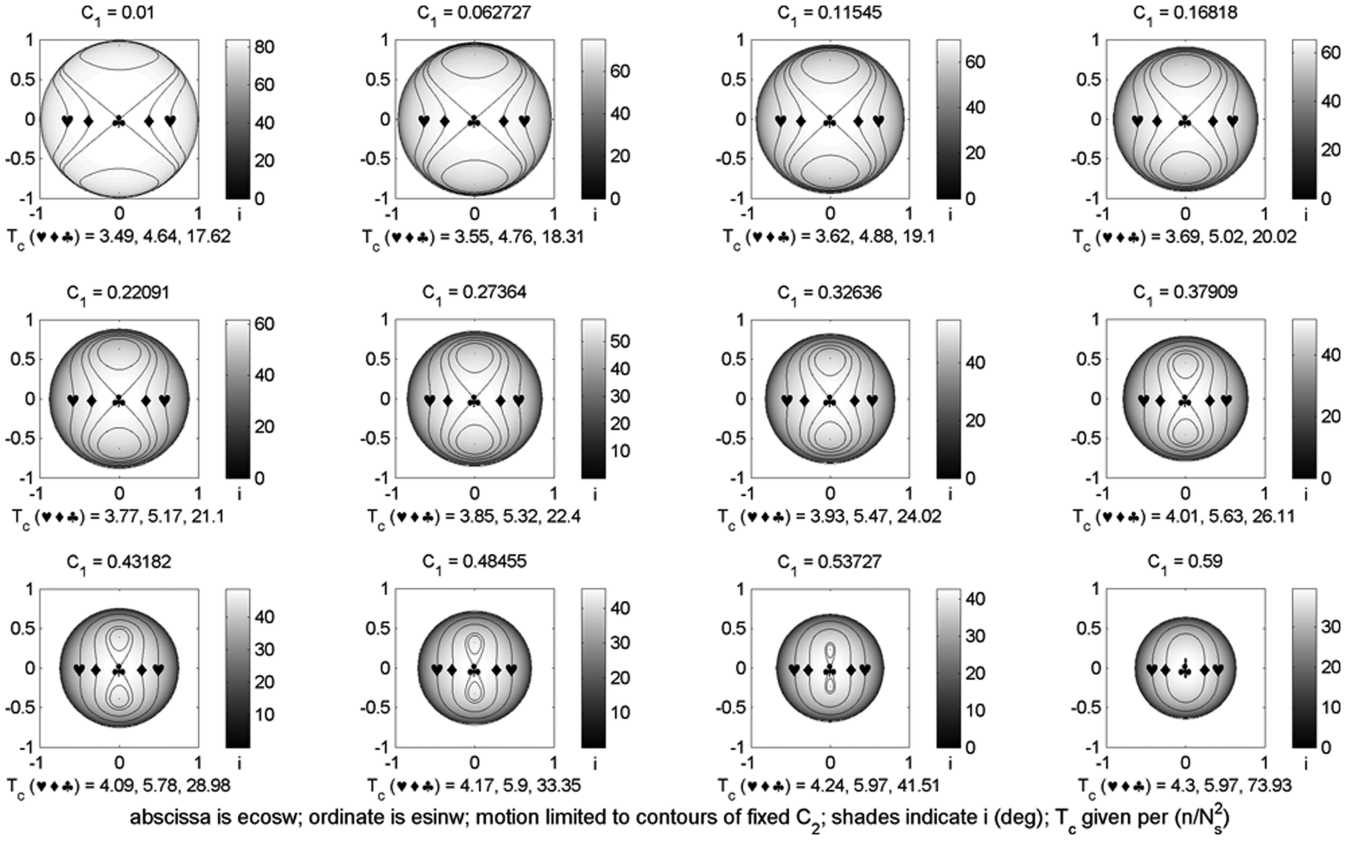

Fig. 3 Overview of postbifurcation motion in the doubly averaged system.

circulating orbit is termed a "figure-eight" orbit due to its contour's shape. Note that it achieves the highest possible inclination of all the circulating orbits and has a C_2 of slightly above zero by definition. For practical consideration, the figure-eight orbits are attractive to the science community for the following reasons:

1) Their circulating nature distributes close approaches through different latitudes and longitudes.

2) They enjoy the maximum possible inclinations of all the circulating orbits.

3) Their long periods and high altitudes enable unique opportunities for planet-system science.

4) They cost less to achieve in comparison with traditional low-altitude circular orbits.

If the initial conditions are the same as the preceding, except $\omega_0 = 90$ deg, the contour librates around just the top island, with a very similar range in i and e. In terms of mission design, a circulating trajectory will find close-approach locations distributed among different latitudes, whereas a librating trajectory will find the close-approach locations centered near the orbit-inclination latitudes on either the northern or southern hemisphere. As seen in Figs. 3 and 4, each circulating contour has an associated full-cycle period, which is defined as the amount of time necessary for the spacecraft to complete one trip around its constant-C_2 curve. A circulating orbit's full-cycle period can be calculated by numerical integration of Eqs. (5–7) or, more simply, from the quadrature given in Eq. (11) using the bounds from Eqs. (12) and (13):

$$T_c = \frac{16}{3}\frac{n}{N_s^2}\int_{e_0}^{e_f} \frac{e\sqrt{1-e^2}}{\sqrt{(2e^2-5C_2)(e^2-1)[3e^4+(5C_1+5C_2-3)e^2-5C_2]}}\,\mathrm{d}e \tag{11}$$

$$e_0 = \sqrt{C_2 5/2} \tag{12}$$

$$e_f = \tfrac{1}{6}\sqrt{6\sqrt{25(C_1^2+C_2^2+2C_1C_2)+30(C_2-C_1)+9}-30(C_1+C_2)+18} \tag{13}$$

An expression for the full-cycle contour period of a librating orbit can be found using a similar procedure; in this case, the eccentricity bounds in Eqs. (14) and (13) are found using the two positive roots of the resulting quartic at $\omega = 90$ deg:

$$e_0 = \tfrac{1}{6}\sqrt{-6\sqrt{25(C_1^2+C_2^2+2C_1C_2)+30(C_2-C_1)+9}-30(C_1+C_2)+18} \tag{14}$$

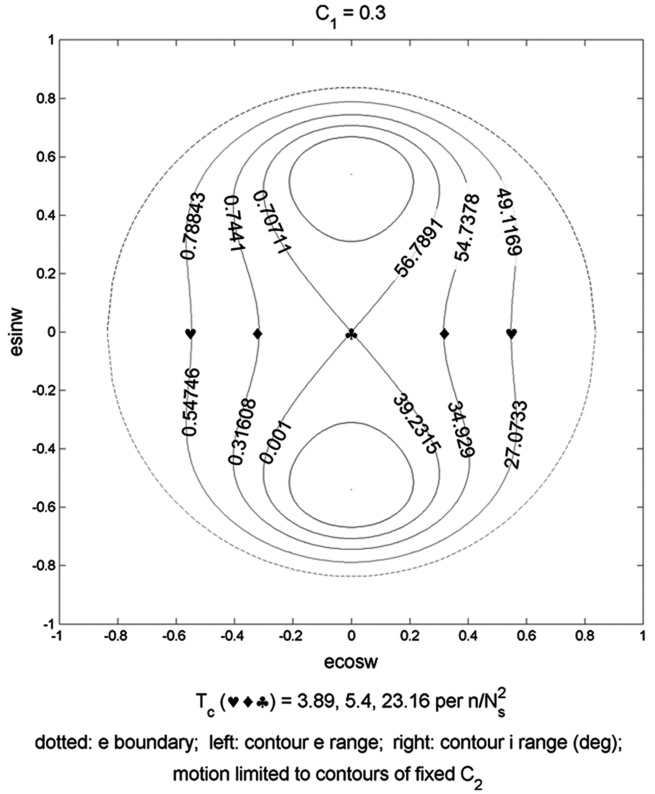

Fig. 4 Sample postbifurcation motion in the doubly averaged third-body problem.

Further, the T_c expression in the librating case is doubled instead of quadrupled because its contour is symmetric only about the y axis, which results in a constant coefficient of $8/3$ instead of $16/3$ in Eq. (11). The quadrature for the full-cycle contour period is derived from Eq. (5) by separating variables; expressing i and ω in terms of e, C_1, and C_2 using Eqs. (9) and (10); simplifying; and integrating both sides. Each circulating contour is symmetric about both the x and y axes; therefore, the eccentricity bounds are found using Eqs. (9) and (10) at $\omega = 0$ and 90 deg, and the T_c expression is accordingly quadrupled. Note that the periods provided in Figs. 3 and 4 are expressed as nondimensioned factors of n/N_s^2, where, in general, the full-cycle period is only a function of n, N_s, C_1, and C_2. The full-cycle period finds its maximum dimensionless value at $C_2 \sim 0$, and a quick and nonlinear reduction in period as a function of initial eccentricity (at $\omega_0 = 0$ deg) is clearly apparent when viewing the cycle period labels in Fig. 3.

Note that each of the eccentricity limits shown in Eqs. (12–14) causes the denominator of the integrand of Eq. (11) to equal zero, which makes the integral in this equation singular. The integral can be shown to converge for all C_1 and C_2 of interest by virtue of comparison tests to known convergent singular integrals [14]. Note that the exact boundaries (see [2]) of valid C_1 and C_2 should be avoided. Further, if $C_1 < 3/5$, then exactly $C_2 = 0$ should be avoided because of singularities associated with the bifurcation between circulating and librating orbits. For practical purposes, the numerical integration of this equation should be performed slightly within the appropriate bounds to avoid these singularities; this method produced very accurate full-cycle period values when compared with corresponding numbers taken from a numerical propagation of Eqs. (5–7).

Based on the premise that the science community prefers high inclinations for favorable mapping and observation purposes, we note in Fig. 3 that the upper bound of inclination on a figure-eight orbit (occurring at $e = 0$) increases for smaller C_1 values. The corresponding upper bound on eccentricity (occurring at $\omega = \pm 90$ deg) also increases for smaller C_1. Therefore, to maximize inclination for a figure-eight orbit around a specific planetary moon, we select a C_1 value such that the upper bound on the eccentricity cycle leads to an orbit with a grazing periapse altitude and an apoapse altitude reaching to the furthest limits of the doubly averaged model validity. The minimum periapse radius is based on the sum of the moon's radius and an assumed 100 km minimum altitude, whereas the maximum apoapse is based on the largest possible radius orbit that remains valid in the doubly averaged model. Equations (15) and (16) express the resulting maximum a and e derived from simple two-body geometry:

$$a_{\max} = a_s \left[\frac{\mu_p}{\mu_s} \left(\frac{T_s}{T} \right)^2 \right]^{-1/3} \tag{15}$$

$$e_{\max} = 1 - \frac{(R + \text{alt}_{\min})}{a_{\max}} \tag{16}$$

Noting that C_1 is constant, the right-hand side of Eq. (9) applied at $\omega = 0$ deg (where $e = 0$ and $i \sim i_{\max}$) can be equated to the same expression applied at $\omega = 90$ deg (where $e = e_{\max}$ and $i \sim 39$ deg). The result is simplified to produce the maximum inclination relationship given in Eq. (17):

$$i_{\max} = \arccos \sqrt{(1 - e_{\max}^2)3/5} \tag{17}$$

Therefore, the figure-eight orbit will oscillate between inclinations of $\sim$39 deg and $i_{\max}$. A figure-eight orbit's C_2 value is always slightly above zero, but C_1 is dependent on the physical parameters of the system and orbiter. Because the maximum inclination occurs at zero eccentricity, Eq. (9) easily reduces to Eq. (18):

$$C_1 = \cos^2 i_{\max} \tag{18}$$

Thus, figure-eight-orbit full-cycle contour-period values for each moon system can be found using Eqs. (11–13) and (15–18) accordingly. Table 2 shows these parameters for several different moon systems in our solar system. Note that the list of systems is taken from [7], in which characteristic instability times are presented for low-altitude circular orbits of potential moons of interest. The data in the first seven columns of Table 2 come from the physical parameters of each system as well as basic orbital mechanics equations, and the data in the last three columns come directly from the equations of the doubly averaged third-body system. Note that the data given in Table 2 are based on figure-eight orbits with very small but nonzero initial e, whereas a realistic trajectory would likely start with a greater eccentricity to avoid the bifurcation to a librating orbit. As mentioned previously and appreciated in Fig. 3, the circulating orbits with larger initial e (for example, 0.1) will find from Eq. (11) significantly shorter full-cycle periods than those reported in Table 2. Although Titan and Triton (for example) are known to have atmospheres and would likely require higher minimum altitudes, for consistency, we choose a periapse altitude of 100 km for each of the moons.

From Table 2, five of the figure-eight science-orbit parameters for each moon system directly depend on the ratio between moon period and spacecraft period (T_s/T). Clearly, the maximum sustainable inclinations for a particular moon system are directly related to the relative size of the third-body perturbation. In general (and as expected), the maximum sustainable inclinations increase for larger moons and moons further from their associated planet. The values presented in Table 2 are based on an order-of-magnitude period ratio, which was stated before as the necessary value to justify the averaging approximation. Negative maximum eccentricities in the table correspond to moon systems that have no possible figure-eight science orbits at this particular period ratio. As the magnitude of period ratio is decreased, maximum eccentricity and maximum inclination change accordingly. The specific trends of this change for the four outer-planet flagship moons[¶] (Europa, Ganymede, Enceladus, and Titan) are shown in Fig. 5 [15].

[¶]Data available online at http://www.lpi.usra.edu/opag/jso_final_report.pdf [retrieved 11 October 2008].

Table 2 Figure-eight science orbits with maximum inclinations[a] for different moon systems

Satellite	μ_s, km^3/s^2	r_p,[b] km	a_s, km	T_s, days	$a_{\max}$,[a] km	$e_{\max}$[a]	C_1[a]	$i_{\max}$,[a] deg	T_c,[a] days
Earth ($\mu_p = 398,479.14$ km^3/s^2)									
Moon	4902.801	1838	384,400	27.46	19,119	0.904	0.110	70.6	832.7
Mars ($\mu_p = 42,815.397$ km^3/s^2)									
Phobos	0.0007158	111	9380	0.32	5	−20.500	−251.57	N/A	N/A
Deimos	0.000098	106	23,460	1.26	7	−14.944	−133.39	N/A	N/A
Jupiter ($\mu_p = 126,649,960$ km^3/s^2)									
Io	5959.916	1922	421,800	1.77	3281	0.414	0.497	45.2	98.0
Europa	3202.739	1661	671,100	3.55	4244	0.609	0.378	52.1	147.4
Ganymede	9887.834	2731	1,070,400	7.16	9856	0.723	0.286	57.6	259.6
Callisto	7179.289	2510	1,882,700	16.69	15,581	0.839	0.178	65.1	537.8
Amalthea	0.138	183	181,400	0.50	40	−3.562	−7.011	N/A	N/A
Thebe	0.1	149	221,900	0.68	44	−2.379	−2.795	N/A	N/A
Adrastea	0.0005	108	129,000	0.30	4	−23.633	−334.52	N/A	N/A
Metis	0.008	122	128,000	0.30	11	−10.063	−60.160	N/A	N/A
Saturn ($\mu_p = 37,918,950$ km^3/s^2)									
Mimas	2.53	299	185,540	0.94	162	−0.843	0.174	N/A	N/A
Enceladus	7.21	352	238,040	1.37	295	−0.195	0.577	N/A	N/A
Tethys	41.21	636	294,670	1.89	653	0.025	0.600	39.3	193.9
Dione	73.113	663	377,420	2.74	1012	0.345	0.528	43.4	172.6
Rhea	154.07	865	527,070	4.52	1812	0.523	0.436	48.7	210.6
Titan	8978.19	2676	1,221,870	15.95	16,286	0.836	0.181	64.8	515.4
Hyperion	0.37	233	1,500,880	21.71	691	0.663	0.336	54.5	843.4
Uranus ($\mu_p = 5,793,962.5$ km^3/s^2)									
Ariel	90.3	679	190,900	2.52	1028	0.340	0.531	43.2	160.9
Umbriel	78.2	685	266,000	4.15	1366	0.499	0.451	47.8	200.4
Titania	235.3	889	436,300	8.72	3234	0.725	0.285	57.8	315.5
Oberon	201.1	861	583,500	13.48	4104	0.790	0.225	61.7	455.8
Miranda	4.4	336	129,900	1.42	256	−0.314	0.541	N/A	N/A
Neptune ($\mu_p = 6,835,130.1$ km^3/s^2)									
Triton	1427.9	1453	354,800	5.87	4531	0.679	0.323	55.4	223.7
Pluto ($\mu_p = 873.66325$ km^3/s^2)									
Charon	108	693	17,536	5.70	1880	0.631	0.361	53.1	230.1

[a]$T_s/T = 10$ [b]$r_p = r + \text{alt}_{\min}$; $\text{alt}_{\min} = 100$ km

The figure-eight orbit maximum eccentricities and inclinations increase as the justifying period ratio decreases. The nominal order-of-magnitude period ratio is an estimate for a justified averaging approximation [7]. The distinction between valid and invalid use of averaging in terms of the period ratio is a fuzzy boundary. We can only state with confidence that applications with period ratios much greater than ∼10 are well modeled by the averaging procedure, and applications with period ratios much less than ∼10 are poorly modeled. Figure 5 shows that a figure-eight orbit is possible for Enceladus** at a period ratio of five, but the spacecraft would violate the minimum altitude constraint at any ratio above ∼7.7. Alternatively, Ganymede, Europa, and Titan enjoy figure-eight orbits with large eccentricities across the entire period-ratio range shown. Previous work that documents families of periodic orbits around planetary moons [3,17] indicates that perturbed Keplerian orbits either cease to exist or find dramatic character changes much beyond roughly 2/5 of the Lagrange point distance, which corresponds to a period ratio of ∼7. Numerical simulations verify that the doubly averaged predictions of the long-period orbital element evolution closely match the full dynamics when the period ratio is at or above ∼10. For smaller period-ratio values, the doubly averaged predictions degrade in accuracy. Note that the Europa maximum inclination line in Fig. 5 is consistent with the findings in [6,18] that suggest that the doubly averaged assumptions break down for eccentric frozen orbits at Europa for inclinations above ∼55 to ∼60 deg.

The high-inclination orbits sought in the current study are naturally relevant to the discussion of capture or escape trajectories, as the breakdown of the doubly averaged assumptions indicate a greater presence of third-body perturbations. In fact, [6] demonstrates that the propulsive maneuver requirements are small for capture to highly inclined elliptic frozen orbits at Europa. Although the frozen orbits from [6] have fixed arguments of periapse, it is speculated that the circulating orbits of the current study will require similarly low-capture Δv maneuvers.†† Because the target exists on a contour rather than a single point, we conjecture that a circulating argument of periapse will be marginally easier to target, compared with a frozen orbit.

Considering Ganymede as an example, Table 2 shows that the doubly averaged system is well suited for predicting motion when the semimajor axis is less than or equal to ∼9856 km. At this semimajor-axis length, a 100-km-minimum-altitude orbiter at Ganymede can sustain rather large eccentricities (up to ∼0.723) without impacting. Further, the large altitudes reduce the sensitivity to nonspherical gravity. Therefore, Ganymede is an excellent application for the doubly averaged circulating and librating trajectories that often lead to large-eccentricity excursions. Accordingly, we design a highly inclined 24 h eccentric orbit at Ganymede (a reference orbit for the Jupiter System Observer flagship study from fiscal year 2007). The 24 h period requires an average semimajor axis of ∼12,320 km. Although this exceeds the just-mentioned formal limit of ∼9856 km, we proceed to test the period-ratio limit of applicability for the doubly averaged system at this particular moon. The 24 h period is synchronous with typical work shifts and is therefore highly desirable in terms of staffing and operations. An orbit is sought with distributed low-altitude close approaches and high inclinations for favorable science geometry. The $C_1 = 0.22$ subplot of Fig. 3 shows a figure-eight contour yielding an oscillating orbit eccentricity that varies between near-circular and ∼0.78 with a maximum inclination of ∼61 deg. This circulating 24 h orbit leads to a 925 × 19,650 km altitude orbit. In the following section, we seek to verify the averaging assumptions by identifying and comparing periodic

**Note that [16] documents stable circulating science orbits at Enceladus with inclinations as high as 65 deg. However, these orbits exist well into the region in which the doubly averaged model fails to predict the unaveraged motion.

††As a check, we verify that the zero-velocity curves in the corresponding three-body problem for the example Ganymede orbits studied in the following section do indeed allow (although just barely) ballistic transport from outside of Ganymede's vicinity.

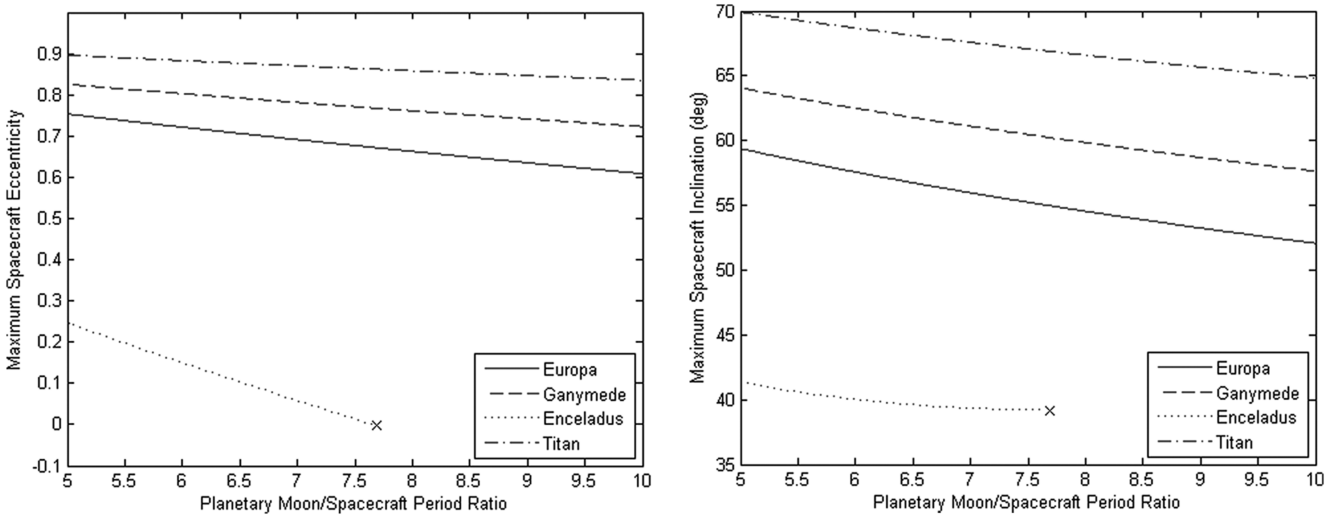

Fig. 5 Maximum inclination and eccentricity as a function of the model justifying period ratio.

orbits in the unaveraged model with similar orbital element evolutions.

IV. Unaveraged Model

A second general technique for analyzing motion near planetary moons involves the search and characterization of periodic orbits in unaveraged models (see [3–5,19–24] for details). The periodic orbits are crucial for characterizing the motion in instances when the doubly averaged assumptions are not valid [3,5,19,22]. In cases inside the region of validity, the periodic orbits provide higher-order solutions.

The local periodic-orbit search is performed in Hill's model superimposed on an $n \times n$ spherical harmonic gravity field. Hill's potential and nonspherical two-body potential are time-invariant and Hamiltonian by nature; therefore, periodic orbits will likely exist and an abundance of well-known fast computational methods apply. A general-use prototype software package called Groove[‡‡] is used to find and analyze periodic orbits and families of orbits. The algorithms and concepts are explained and demonstrated in [4,20,21].

Starting with the initial conditions

$$\{a_0 = 12,320 \text{ km}, \quad i_0 = 60\,\text{deg}, \quad e_0 = 0.1,$$
$$\omega_0 = \Omega_0 = \upsilon_0 = 0\,\text{deg}\}$$

the unaveraged equations (including the nonspherical terms) are propagated until a full circulation in the e–ω plane completes. For this example, it requires approximately 81 revolutions. We therefore seek a periodic orbit that closes in the body-fixed frame after 81 revolutions. The ~80-day period is consistent with the 70.3-day period calculated using the quadrature from Eq. (11). The differential corrector converges to the initial conditions given in Table 3.

The natural family of similar orbits is then found by targeting neighboring Jacobi-constant values. The effect of changing the Jacobi constant on this family in the vicinity of the orbit of interest is small changes in average inclination. Figure 6 shows the family of orbits as a function of average inclination. The 12:81 family indicates that the spacecraft makes 81 revolutions, whereas Ganymede makes $12 + \Delta\Omega$ revolutions before closing the periodic orbit in the body-fixed frame. The ratio of the two integers can be adjusted to change the average semimajor axis [4].

[‡‡]The Groove software package (developed primarily at the Jet Propulsion Laboratory, written in FORTRAN 90) represents a new capability for the rapid design of science orbits and can benefit missions desiring global surface coverage, maximum orbital stability, predictable orbital elements, sun synchronicity, and/or high-fidelity repeat ground tracks. Example applications include, but are not limited to, Europa, Ganymede, Enceladus, Vesta, the moon, Earth, and Mars.

The stability indices b_1 and b_2, calculated from the Monodromy (full-period state transition) matrix in Fig. 6 must both be less than or equal to 2 for linear stability [25]. We remark that b_2 is equal to 2 for the domain illustrated, a common feature of many revolution periodic orbits. Because b_1 is (mildly) greater than 2, the orbits of Fig. 6 are therefore mildly unstable, indicating that the exact repeat ground tracks will eventually be destroyed when propagated for long periods. The implications of the instability will be further investigated with ephemeris propagations in a later section. The stated periodicity is a measure of how closely the targeted final state matches the initial state, and 10^{-q} is roughly equivalent to matching q significant digits.

To demonstrate the properties of a particular orbit, Figs. 7–9 show characteristics of an example 12:81 periodic orbit propagated for one period. The three-body nature of the orbit is appreciated in the large variations seen in the osculating orbital elements shown in Fig. 7. The orbit has altitudes ranging from ~1000–18,500 km, eccentricities ranging from 0.02–0.7, and inclinations ranging from 45–62 deg. The argument of periapse is clearly of the circulating nature, as it cycles exactly once in the ~78-day period. The quickly precessing and librating orbits are appropriately coined "ball-of-yarn" orbits, as the body-fixed trajectory plot in Fig. 7 illustrates. The repeat ground tracks and the associated close-approach locations are illustrated in Fig. 8. The figure-eight path of the eccentricity vector in Fig. 9 clearly resembles the circulating contours predicted from the doubly averaged system.

It is emphasized that the family shown in Fig. 6 is simply one of several possible similar families. To illustrate, we also show a similar

Table 3 Example periodic orbits in Hill's model plus 4 × 4 Ganymede gravity field [a]

Property	Units	12:81 unstable orbit	9:56 stable orbit
x_0	km	−1.10294724E + 04	1.27215637E + 04
y_0	km	6.09916977E + 02	2.74572065E + 03
z_0	km	−9.92043402E − 15	0.00000000E + 00
u_0	km/s	−2.56020704E − 02	−5.19574390E − 01
v_0	km/s	−4.71573204E − 01	3.16290562E − 01
w_0	km/s	8.73907974E − 01	6.25411458E − 01
a_0	km	1.23072793E + 04	1.30393130E + 04
e_0	——	1.02457203E − 01	5.05659039E − 01
i_0	deg	6.16128288E + 01	5.61929409E + 01
ω_0	deg	2.94588490E − 01	1.20188898E + 02
Ω_0	deg	1.76834834E + 02	1.21794367E + 01
υ_0	deg	−2.94588490E − 01	−1.20188898E + 02
T_c	day	7.75866851E + 01	5.70386714E + 01
Average i	deg	56.18	56.22

[a]Initial conditions given in the nonrotating frame aligned with the IAU-defined Ganymede body-fixed frame at epoch.

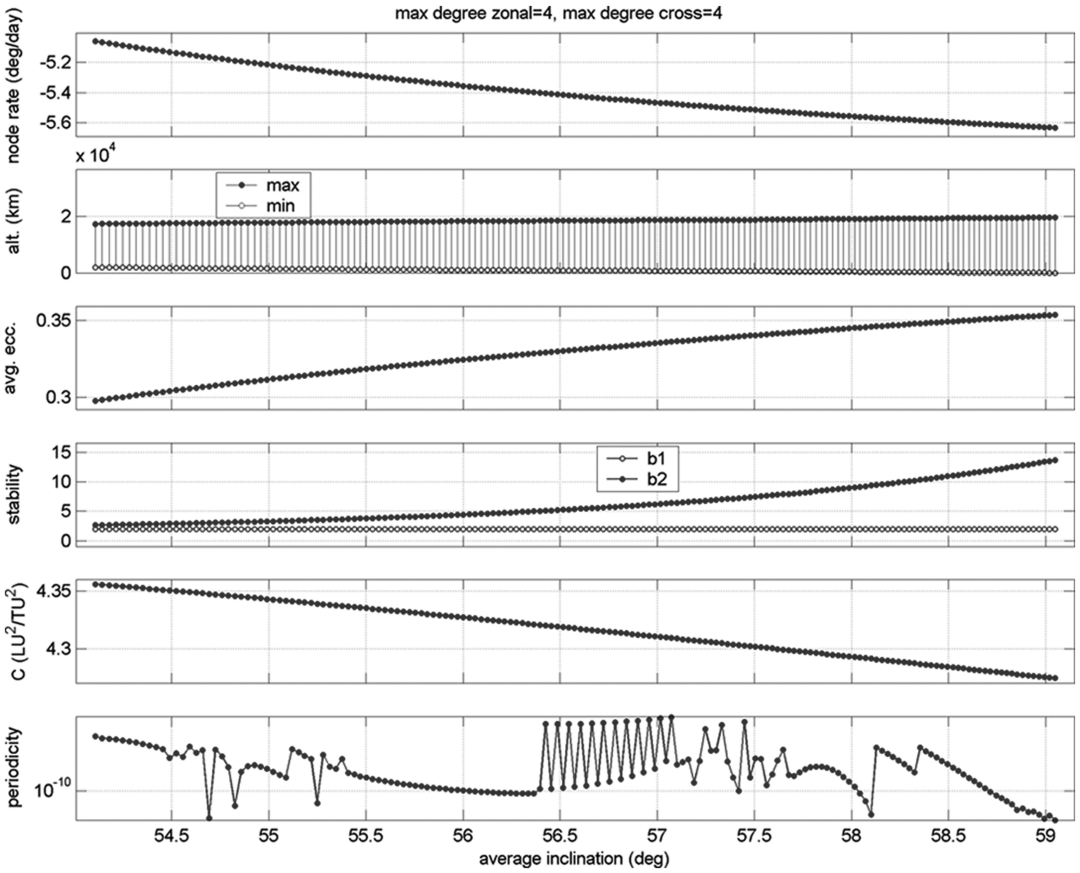

Fig. 6 Promising family (12:81) of science orbits at Ganymede. ($b_2 = 2$ for full domain).

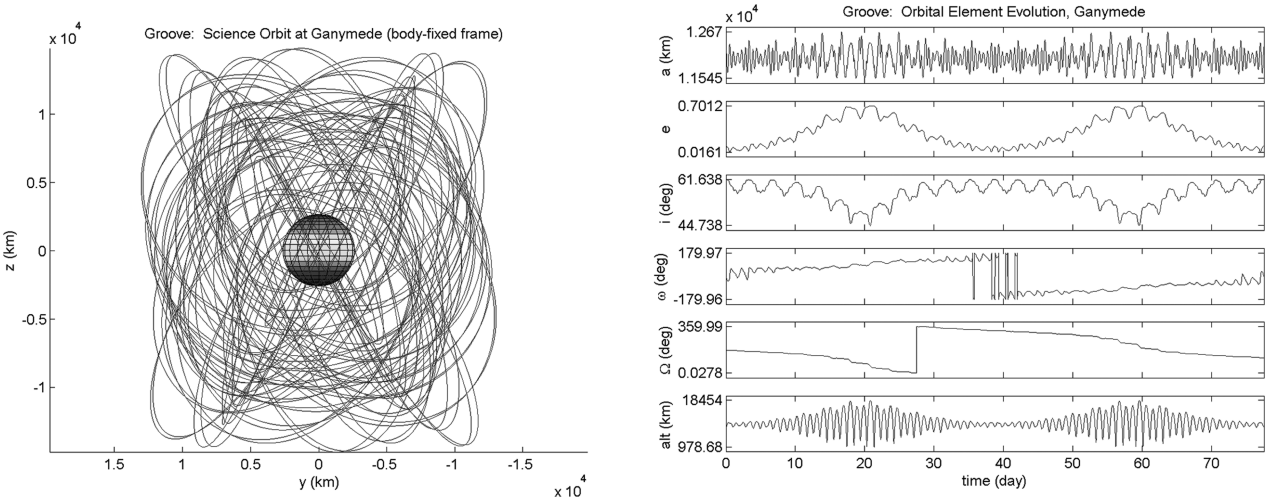

Fig. 7 One period of example 12:81 science orbit: trajectory (left) and orbital elements (right).

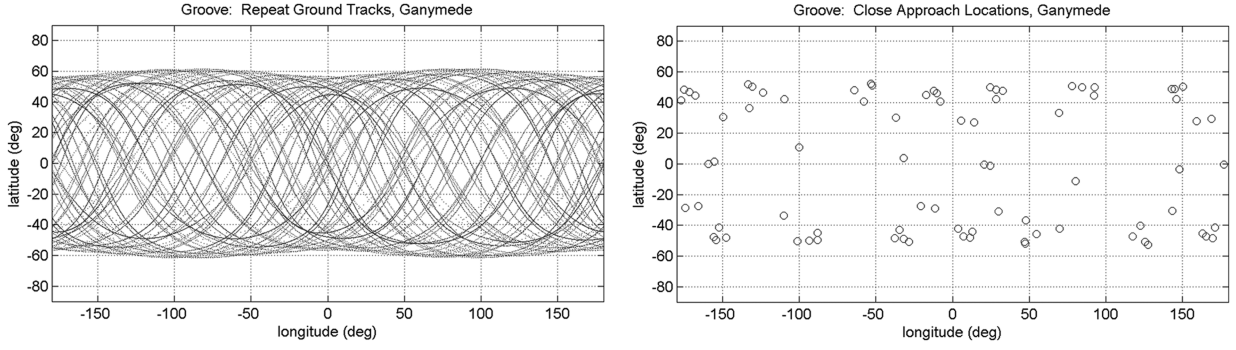

Fig. 8 One period of example 12:81 science orbit: ground tracks.

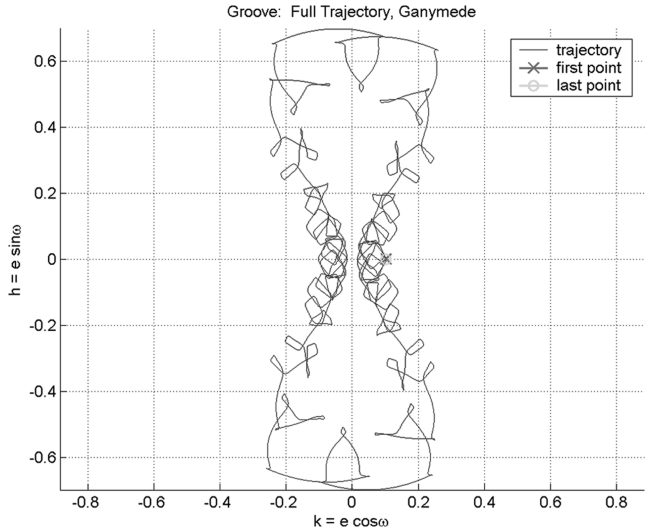

Fig. 9 One period of example 12:81 science orbit: eccentricity vector repeat path.

family of orbits with slightly lower periapses and larger periods (closer to the target 24 h) in Fig. 10. Note that contrary to the 12:81 family (although both families are very similar in nature), all of the orbits shown in Fig. 6 of the 9:56 family are linearly stable, as indicated by both stability indices being less than or equal to 2. Therefore, in this model, the exact repeat orbits will remain intact over long propagations. An example 9:56 orbit is illustrated in Figs. 11–13. Note that the full-cycle period of the 9:56 (∼57 days) orbit is substantially less than that of the 12:81 (∼78 days) orbit. This result is consistent with the doubly averaged model, in which an increasing neck size of the figure-eight path corresponds with a smaller full-cycle period (see Figs. 9 and 13).

V. Long-Term *N*-Body Propagations

The important consideration of nonconservative perturbations (the realistic ephemeris for example) and force-model uncertainties also play key roles in the detailed stability analysis and design of science orbits at planetary moons. For examples of previous studies that address the transition from simplified dynamics to ephemeris models, see [4,19–21,26].

The stable solutions discussed in this study are considered to be linearly stable in the conservative force model, including the Hill third-body perturbation and the nonspherical Ganymede gravity terms. The radius of the stability regions around the stable orbits in the presence of numerical and other perturbations is unclear. Unstable orbits such as those of the 12:81 family may or may not be robust to realistic perturbations in terms of mission design. If the exact repeat pattern is destroyed yet the eccentricity keeps circulating with the same ranges, the instability is of little consequence. However, we have already demonstrated that the 24 h orbit is likely pushing the boundaries of applicability for the doubly averaged dynamics, and further investigations are therefore necessary.

Although not implemented here, methods using fast Lyapynov indicators are useful for estimating stability region radii [19,26]. Instead, we rely on ephemeris *n*-body propagations as a simple and crude approach to measure the stability robustness of a particular solution to nontrivial perturbations. We proceed by propagating the two example orbits in ephemeris simulations involving two-body gravity from the sun, Jupiter, Saturn, and all the Galilean moons, as well as oblateness effects from Jupiter and Ganymede. By specifying the initial conditions given in Table 3 in the body-fixed frame at

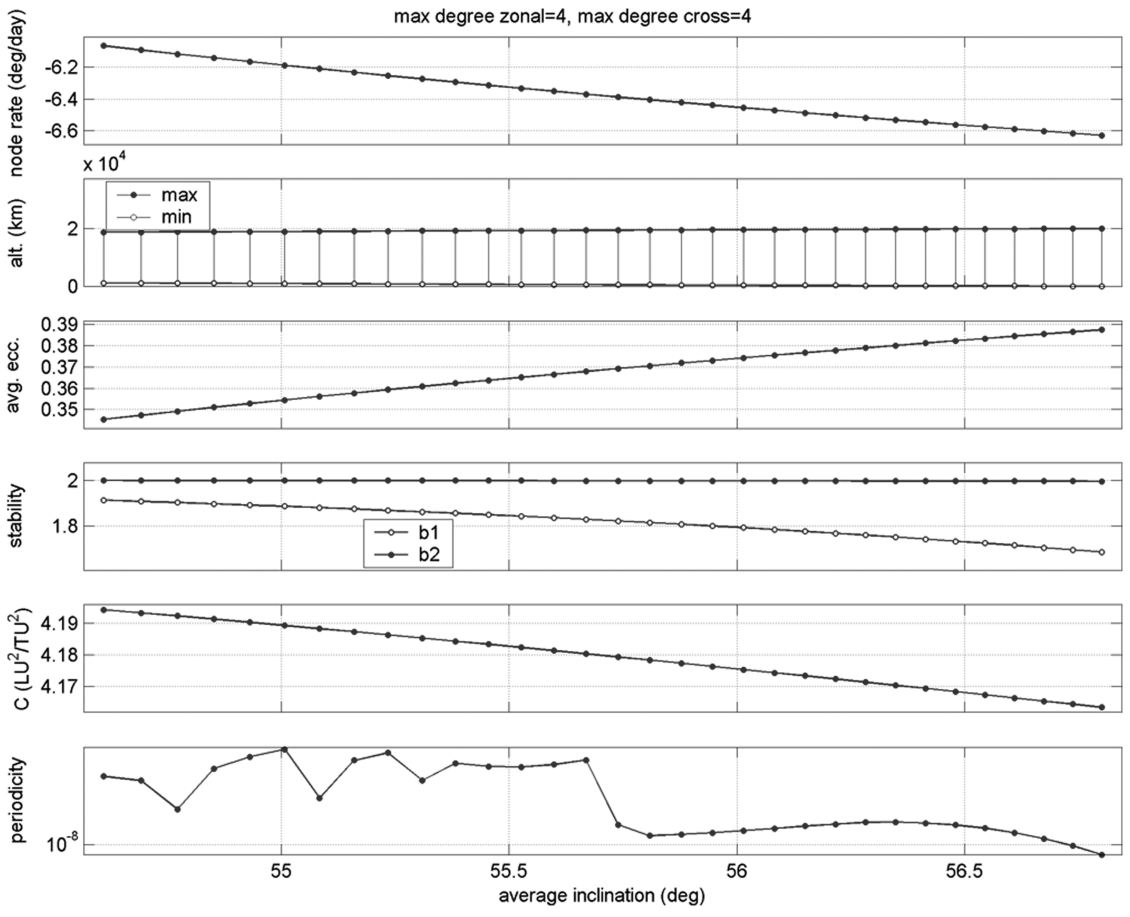

Fig. 10 Promising family (9:56) of science orbits at Ganymede.

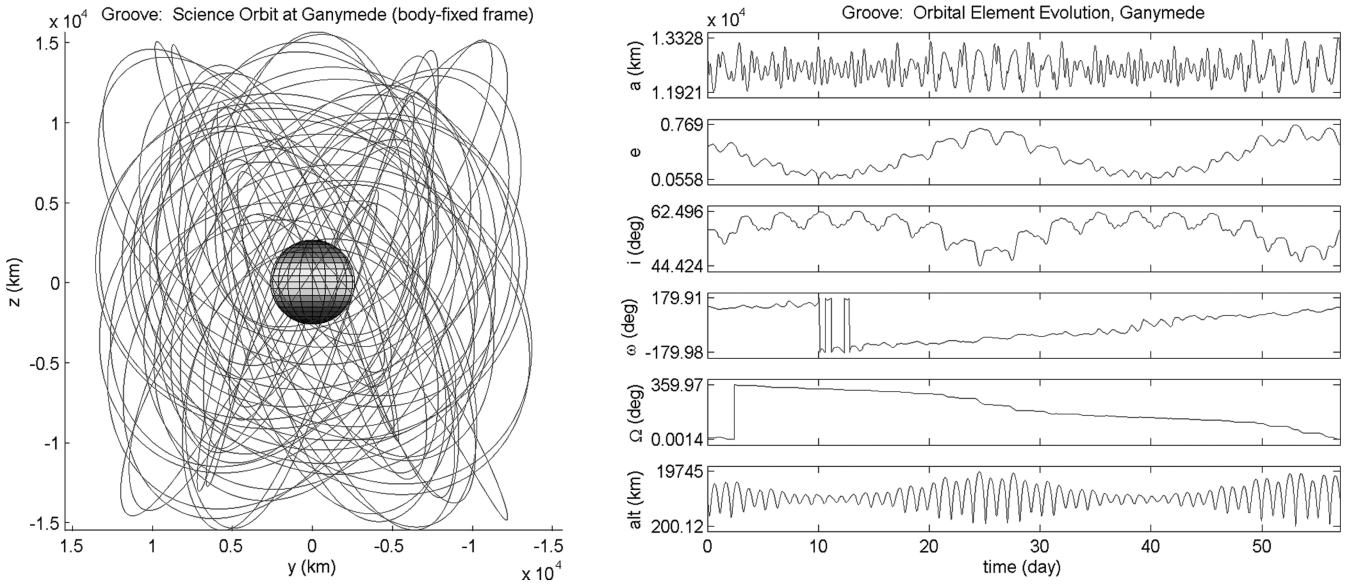

Fig. 11 One period of example 9:56 science orbit: trajectory (left) and orbital elements (right).

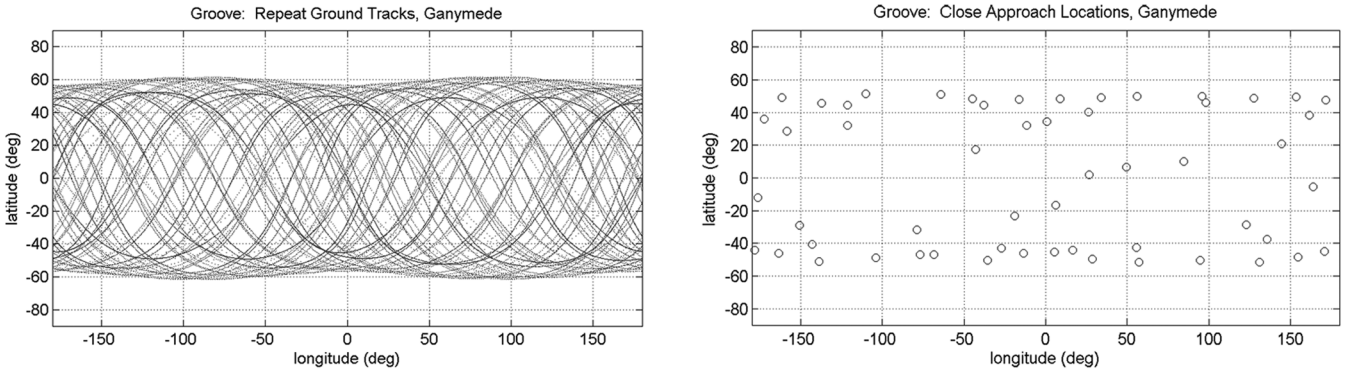

Fig. 12 One period of example 9:56 science orbit: ground tracks.

epoch, propagations beginning at arbitrary epochs have the effect of sampling uncertainties in the force model. If a particular orbit maintains its basic characteristics without impacting or escaping for 1 year starting at 10 arbitrarily chosen epochs, it is considered to be long-term stable.

Figures 14–16 show characteristics of the 9:56 example-orbit ephemeris propagation. The epoch is arbitrarily chosen as 1 January 2028 (Julian date of 2,461,772.0). This orbit is deemed to be long-term stable, as each of the 10 different epochs led to orbital lifetimes of at least 1 year. By comparing the eccentricity vector path and the close-approach locations of the simplified-model equivalent orbit, it is clear that basic orbital characteristics are maintained during the long-term propagation. It should be noted from Fig. 11 that the example orbit has a minimum altitude of ∼200 km in the simplified model, and Fig. 16 shows consistency in the long-term ephemeris propagations. Because the orbits from family 12:81 are unstable in the simplified model, the example from Fig. 7 is chosen with a higher minimum altitude of ∼1000 km in anticipation of a less robust solution to the realistic perturbations. Although we do not explicitly illustrate the propagations, the 12:81 orbit also passes the long-term stability test for 10 ephemeris propagations with arbitrary epochs. As predicted, however, the unstable 12:81 orbits lead to less repeatability in the ephemeris propagations, and subsequently the minimum altitudes dip down to ∼250 km, as compared with the ∼1000 km in the conservative model.

A brief analysis was performed to spot-check the sensitivity of the long-term propagation to the nonspherical gravity of Ganymede. The same stability test of applying 10 arbitrary epochs led to similar long-term stable results using only a Ganymede point mass. Although this result is promising and certainly due to the large altitudes compared with the Ganymede radius, considerable future work is required to understand the nonspherical gravity-field implications.

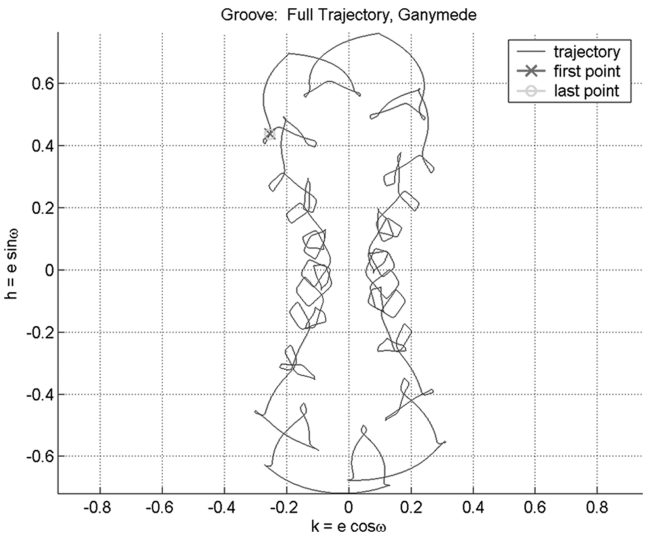

Fig. 13 One period of example 9:56 science orbit: eccentricity vector repeat path.

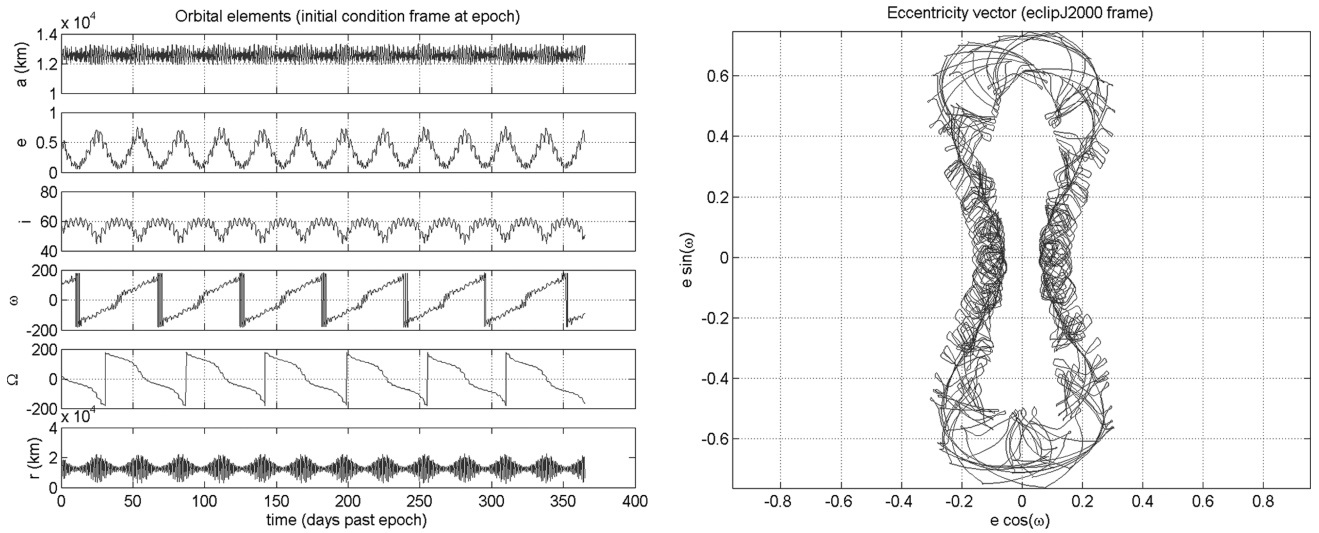

Fig. 14 Long-term *n*-body ephemeris propagation for 9:56 orbit: orbital elements evolution (left, angles in deg) and eccentricity vector repeat path (right).

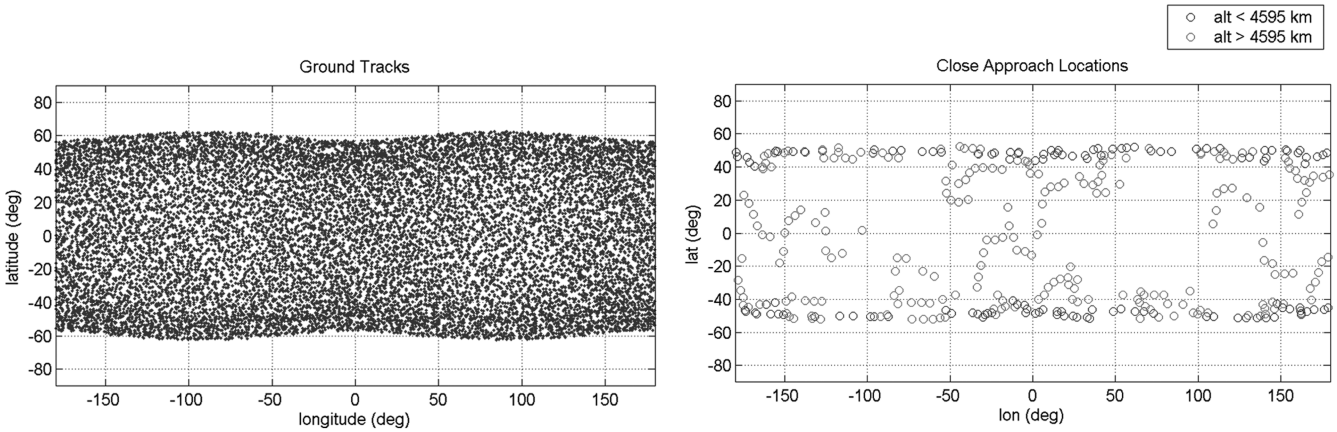

Fig. 15 Long-term *n*-body ephemeris propagation for 9:56 orbit: Ground tracks.

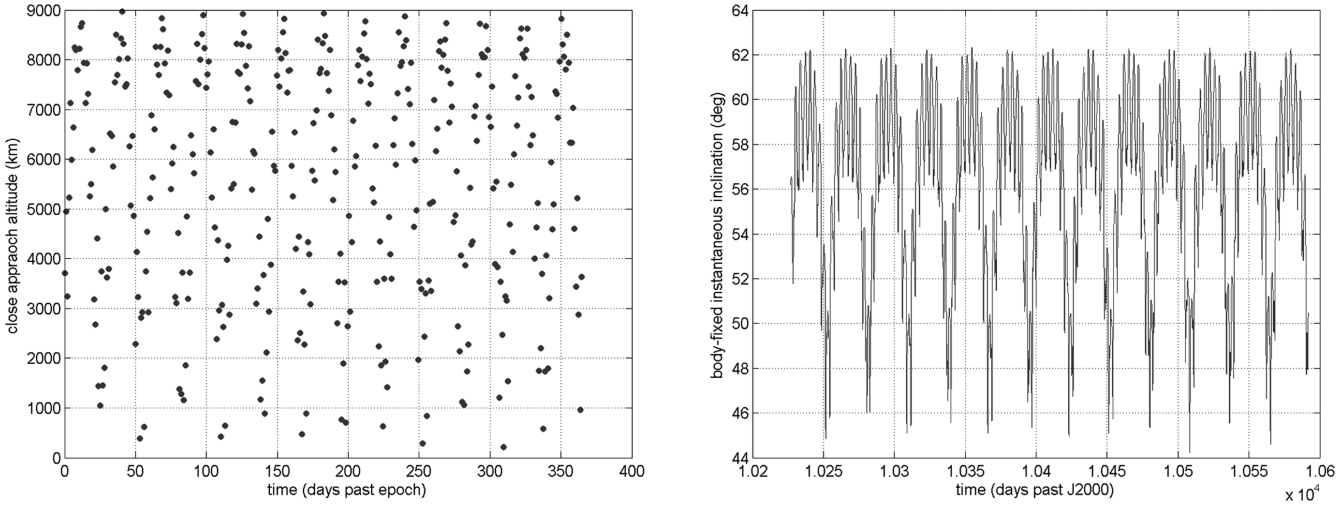

Fig. 16 Long-term *n*-body ephemeris propagation for 9:56 orbit: close-approach distances (left) and body-fixed *i* (right).

VI. Conclusions

The first-order effect of the doubly averaged third-body perturbation on a spacecraft near a planetary moon is reviewed, and a detailed contour-plot analysis depicts all types of feasible motion. An emphasis is placed on eccentric orbits and mission-design applications. In particular, the class of orbits that oscillate between near-circular and highly eccentric and include a circulating argument of periapse is introduced as a viable, high-science-value, low-cost trajectory design for planetary-moon missions. These circulating figure-eight orbits are evaluated and documented in the

Table A1 Representative Ganymede gravity field

J(2) = 5.911042930573900E-05	C(3, 1) = −6.863916460740865E-06	S(4, 1) = 5.830284294524415E-06
J(3) = −3.921720290616328E-07	S(3, 1) = −5.971806445404929E-06	C(4, 2) = −9.205006749291541E-07
J(4) = 1.619380392450006E-06	C(3, 2) = −6.481431518636326E-06	S(4, 2) = −7.719921073220343E-06
C(2, 1) = −1.089379888322607E-08	S(3, 2) = 1.019584456216980E-05	C(4, 3) = 1.807800500915109E-06
S(2, 1) = −1.204834981027450E-06	C(3, 3) = −7.575116779515599E-06	S(4, 3) = 3.883084011103666E-06
C(2, 2) = 6.152429561579210E-05	S(3, 3) = −8.279091297771898E-07	C(4, 4) = 3.101357600870122E-07
S(2, 2) = −5.410422638487023E-06	C(4, 1) = 4.018167872716952E-06	S(4, 4) = 5.656462546498310E-06

context of maximizing sustainable inclinations for a variety of relevant moon systems. Although the high-eccentricity excursions occur at the lower bound of the inclination cycle, the orbits serendipitously spend the majority of their time at the higher inclinations. Quadrature expressions are derived for quick calculation of the full-cycle periods.

Although the doubly averaged system provides general insight to the third-body problem, we also rely on the periodic orbits in the unaveraged system for higher-order solutions and validation of the doubly averaged predictions. As an example, two families of highly resonant periodic orbits are demonstrated in the unaveraged Hill-plus 4×4 Ganymede gravity-field model. Despite the fact that the orbit period of $\sim$24 h is found to be just beyond the formal region of validity for the doubly averaged assumptions, the example orbits find general agreement with the doubly averaged predictions. The nonspherical gravity terms are found to have nondominant effects on the high-altitude highly eccentric orbits. Finally, long-term ephemeris propagations are used to test the robustness of the example orbits to realistic perturbations. The example orbit from the 9:56 family is stable in the unaveraged model and finds best agreement when transitioning to the full ephemeris.

Considering all possible high-altitude Ganymede orbits with occasional low-altitude close approaches, the proposed Ganymede science orbit enjoys inclinations that are likely at or near the maximum attainable for long-term stable motion. The orbit is circulating with close approaches distributed among all longitudes and ± 62 deg latitude and it cycles between near-circular (9000 km altitude) and highly eccentric ($200 \times 20,000$ km altitude) approximately once a month. The high altitudes compared with the body radius make both poles viewable at near-nadir pointing angles. The highly eccentric orbit is less expensive to achieve than a low-altitude circular orbit, and the orbital geometry and timing are favorable for Ganymede science as well as a variety of Jupiter system science.

In this study, the circulating eccentric orbit is demonstrated in most detail for the Ganymede case. However, the general class of third-body perturbed orbits is a cost-effective option for orbiting any modest-sized planetary moon. Because the orbits of interest are loosely bound in a Keplerian sense, they are naturally obvious targets for designing low-energy capture and escape orbits.

Appendix A: Ganymede Gravity Field

Table A1 gives representative *normalized* gravity-field coefficients for Ganymede originating from Galileo flyby data. The coefficients were used for the Jupiter Icy Moons Orbiter (JIMO) trajectory studies at the Jet Propulsion Laboratory.

Acknowledgments

Part of this work was carried out at the Jet Propulsion Laboratory, California Institute of Technology, under a contract with NASA. The authors thank Johnny Kwok, Nathan Strange, Jon Sims, Grace Tan-Wang, Tom Spilker, and David Senske for their interest in and support of the project.

References

[1] Ely, T., "Stable Constellations of Frozen Elliptical Inclined Lunar Orbits," *Journal of the Astronautical Sciences*, Vol. 53, No. 3, 2005, pp. 301–316.

[2] Broucke, R., "Long-Term Third-Body Effects via Double Averaging," *Journal of Guidance, Control, and Dynamics*, Vol. 26, No. 1, 2003, pp. 27–32.
doi:10.2514/2.5041

[3] Russell, R. P., "Global Search for Planar and Three-dimensional Periodic Orbits Near Europa," *Journal of the Astronautical Sciences*, Vol. 54, No. 2, 2006, pp. 199–226.

[4] Russell, R. P., and Lara, M., "Long-Life Lunar Repeat Ground Track Orbits," *Journal of Guidance, Control, and Dynamics*, Vol. 30, No. 4, 2007, pp. 982–993.
doi:10.2514/1.27104

[5] Lara, M., and San-Juan, J. F., "Dynamic Behavior of an Orbiter Around Europa," *Journal of Guidance, Control, and Dynamics*, Vol. 28, No. 2, 2005, pp. 291–297.
doi:10.2514/1.5686

[6] Paskowitz, M. E., and Scheeres, D. J., "Robust Capture and Transfer Trajectories for Planetary Satellite Orbiters," *Journal of Guidance, Control, and Dynamics*, Vol. 29, No. 2, 2006, pp. 342–353.
doi:10.2514/1.13761

[7] Scheeres, D. J., Guman, M. D., and Villac, B. F., "Stability Analysis of Planetary Satellite Orbiters: Application to the Europa Orbiter," *Journal of Guidance, Control, and Dynamics*, Vol. 24, No. 4, 2001, pp. 778–787.
doi:10.2514/2.4778

[8] Tapley, B. D., Schutz, B. E., and Born, G. H., *Statistical Orbit Determination*, Elsevier Academic Press, Burlington, MA, 2004. Sec. 2.3.

[9] Battin, R. H., *An Introduction to the Mathematics and Methods of Astrodynamics*, AIAA, New York, 1987, p. 483.

[10] Seidelmann, P. K., Abalakin, V. K., Bursa, M., Davies, M. E., Bergh, C. de, Lieske, J. H., Oberst, J., Simon, J. L., Standish, E. M., Stooke, P., and Thomas, P. C., "Report of the IAU/IAG Working Group on Cartographic Coordinates and Rotational Elements of the Planets and Satellites: 2000," *Celestial Mechanics and Dynamical Astronomy*, Vol. 82, No. 1, 2002, pp. 83–111.
doi:10.1023/A:1013939327465

[11] Paskowitz, M. E., and Scheeres, D. J., "Design of Science Orbits About Planetary Satellites: Application to Europa," *Journal of Guidance, Control, and Dynamics*, Vol. 29, No. 5, 2006, pp. 1147–1158.
doi:10.2514/1.19464

[12] Kwok, J. H., "Long-Term Orbit Prediction Using an Averaging Method," AIAA Paper 84-1985, Aug. 1985.

[13] Kwok, J. H., "Doubly Averaging Method for Third Body Perturbations," American Astronautical Society Paper 91-464, Aug. 1991.

[14] Greenberg, M. D., *Foundations of Applied Mathematics*, Prentice–Hall, Englewood Cliffs, NJ, 1978, pp. 51–59.

[15] Spilker, T. R., Senske, D. A., Prockter, L., Kwok, J. H., and Tan-Wang, G. H., "Scientific Investigation of the Jovian System: The Jupiter System Observer Mission Concept," *Bulletin of the American Astronomical Society*, Vol. 39, No. 3, 2007, p. 466.

[16] Russell, R. P., and Lara, M., "On the Design of an Enceladus Science Orbit," AAS/AIAA Astrodynamics Specialist Conference and Exhibit, AIAA Paper 2008-7072, Honolulu, HI, Aug. 2008.

[17] Henon, M., "Numerical Exploration of the Restricted Problem 5: Hill's Case: Periodic Orbits and Their Stability," *Astronomy and Astrophysics*, Vol. 1, 1969, pp. 223–238.

[18] Paskowitz, M. E., and Scheeres, D. J., "Orbit Mechanics about Planetary Satellites," Space Flight Mechanics Meeting, American Astronautical Society Paper 04-244, Maui, HI, Feb. 2004.

[19] Lara, M., Russell, R., and Villac, B., "On Parking Solutions Around Europa," 2005 AAS/AIAA Astrodynamics Specialist Conference, American Astronautical Society Paper 2005-384, Lake Tahoe, CA, Aug. 2005.

[20] Lara, M., and Russell, R. P., "On the Design of a Science Orbit about Europa," 16th AAS/AIAA Space Flight Mechanics Conference, American Astronautical Society 06-168, Tampa, FL, Jan. 2006.

[21] Lara, M., and Russell, R. P., "On the Computation of a Science Orbit about Europa," *Journal of Guidance, Control, and Dynamics*, Vol. 30, No. 1, 2007, pp. 259–263.
doi:10.2514/1.22493

[22] Lara, M., Russell, R. P., and Villac, B., "Classification of the Distant Stability Regions at Europa," *Journal of Guidance, Control, and Dynamics*, Vol. 30, No. 2, 2007, pp. 409–418. doi:10.2514/1.22372

[23] Lara, M., "Searching for Repeating Ground Track Orbits: A Systematic Approach," *Journal of the Astronautical Sciences*, Vol. 47, 1999, pp. 177–188.

[24] Lara, M., "Repeat Ground Track Orbits of the Earth Tesseral Problem as Bifurcations of the Equatorial Family of Periodic Orbits," *Celestial Mechanics and Dynamical Astronomy*, Vol. 86, No. 2, 2003, pp. 143–162. doi:10.1023/A:1024195900757

[25] Broucke, R., "Stability of Periodic Orbits in the Elliptic, Restricted Three-Body Problem," *AIAA Journal*, Vol. 7, No. 6, 1969, pp. 1003–1009. doi:10.2514/3.5267

[26] Lara, M., Russell, R. P., and Villac, B., "Fast Estimation of Stable Regions in Real Models," *Meccanica*, Vol. 42, No. 5, Oct. 2007, pp. 511–515. doi:10.1007/s11012-007-9060-z